Journal of
Ship&Ocean
Technology
MARCH 2004

SOTECH Vol. 8, No. 1, pp. 31~41, 2004

Propulsive Performance Analysis of Ducted Marine Propulsors with Rotor-Stator Interaction

Jin-Ho Jang[1], Hye-Ran Yu[1], Young-Rae Jung[2] and Warn-Gyu Park[1]

[1]School of Mechanical Engineering, Pusan National University, Busan 609-735, KOREA;
E-mail: pusan@pusan.ac.kr
[2]Agency for Defense Development, P.O. Box 18, Jinhae, Kyungnam 645-600, KOREA

Abstract

A ducted marine propulsor has been widely used for the thruster of underwater vehicles for protecting collision damage, increasing propulsive efficiency, and reducing cavitation. Since a single-stage ducted propulsor contains a set of rotor and stator inside an annular duct, the numerical analysis becomes extremely complex and computationally expensive. However, the accurate prediction of viscous flow past a ducted marine proplusor is essential for determining hydrodynamic forces and the propulsive performances. To analyze a ducted propulsor having rotor-stator interaction, the present work has solved 3D incompressible RANS equations on the sliding multiblocked grid. The flow of a single stage turbine flow was simulated for code validation and time averaged pressure coefficients were compared with experiments. Good agreement was obtained. The hydrodynamic performance coefficients were also computed.

Keywords: ducted marine propulsor, rotor-stator interaction, RANS equations, sliding multiblock technique, hydrodynamic performances.

1 Introduction

A ducted marine propulsor has been widely used for the thruster of underwater vehicles, such as submarine and torpedo. The duct has been used to protect the propeller from collision damage, to increase propulsive efficiency, and to reduce cavitation. Since a single-stage ducted propulsor contains a set of rotor and stator inside an annular duct, the numerical analysis becomes extremely complex and computationally expensive. However, the accurate prediction of viscous flow past a ducted marine proplusor is essential for determining cavitation inception, hydrodynamic forces, and the propulsive performances. The previous works of experiments (Zierke et al, 1995 ; 1996) and computations (Hassan et al, 1995 ; Lee et al, 1994 ; Sheng et al, 1997) have been mostly carried out without the duct, although some panel codes (Kerwin et al, 1987, Kinnas and Coney, 1992 ; Huges, 1993) included the duct. The inviscid panel method is efficient and mature method for predicting performances of marine propeller. However, since the flowfield around a ducted propeller involving vortex interactions between a rotor and a stator, and flow interactions

of the boundary layer of duct and vortices is a very complicated three-dimensional viscous flow, Navier-Stokes equation solver should be used to provide a more thorough understanding of the flow features. Most of viscous flow analyses with rotor-stator interactions are limited to the flows of turbine or axial pumps. To authors' knowledge, the CFD work has rarely been applied to the viscous flow of marine propulsor which has a set of rotor and stator, inside of an annular duct(Chen and Whitfield, 2000). This shape of propulsor is usually used for submarine and torpedo.

In the present work, 3D incompressible RANS equations have been solved on the nonorthogonal multiblocked grid system to analyze the flow of ducted marine propulsor. To handle the relative motion between the rotor and the stator, the sliding multiblock method was applied.

2 Governing equations and numerical method

The three-dimensional incompressible Navier-Stokes equations in a generalized curvilinear coordinate system (τ,ξ,η,ζ) may be written as :

$$\frac{\partial \hat{q}}{\partial t}+\frac{\partial}{\partial \xi}\left(\hat{E}-\hat{E}_v\right)+\frac{\partial}{\partial \eta}\left(\hat{F}-\hat{F}_v\right)+\frac{\partial}{\partial \zeta}\left(\hat{G}-\hat{G}_v\right)=0 \tag{1}$$

where $\hat{q}=[0,u,v,w]/J$. $\hat{E}$, $\hat{F}$, and $\hat{G}$ are the convective flux terms. $\hat{E}_v$, $\hat{F}_v$, and $\hat{G}_v$ are viscous flux terms. Eq.(1) is solved by so called iterative time marching method (Park et al, 1991 ; 1993 ; 1996 ; 1998). The solution procedure is briefly reproduced here. Since the momentum equation is a parabolic type of partial differential equation, it can be solved by the time marching scheme as follows :

$$\frac{1}{\Delta\tau}\left(\overline{q}^{n+1}-\overline{q}^{n}\right)+\delta_\xi\overline{E}^{n+1}+\delta_\eta\overline{F}^{n+1}+\delta_\zeta\overline{G}^{n+1}=\delta_\xi\overline{E}_v^{n+1}+\delta_\eta\overline{F}_v^{n+1}+\delta_\zeta\overline{G}_v^{n+1} \tag{2}$$

The barred quantities denote the column vector matrices consisting of momentum equations only. The superscript denotes the physical time level. The operators, δ_ξ , δ_η , and δ_ζ represent spatial differences in ξ-, η-, and ζ-direction, respectively. If Newton iteration method is applied, Eq. (2) is given by

$$\begin{aligned}&\frac{1}{\Delta\tau}\left(\overline{q}^{n+1,k+1}-\overline{q}^{n}\right)+\delta_\xi\overline{E}^{n+1,k+1}+\delta_\eta\overline{F}^{n+1,k+1}+\delta_\zeta\overline{G}^{n+1,k+1}\\&=\delta_\xi\overline{E}_v^{n+1,k+1}+\delta_\eta\overline{F}_v^{n+1,k+1}+\delta_\zeta\overline{G}_v^{n+1,k+1}\end{aligned} \tag{3}$$

where the second superscript, 'k+1', means the iteration level. Following a local linearization of $\overline{E}$, $\overline{F}$, $\overline{G}$, $\overline{E}_v$, $\overline{F}_v$, and $\overline{G}_v$ at 'n+1' time level and 'k' iteration level,

$$\left(\frac{I}{\Delta\tau}+\frac{\partial}{\partial\xi}A+\frac{\partial}{\partial\eta}B+\frac{\partial}{\partial\zeta}C\right)\Delta\overline{q}=\omega\overline{R}^{n+1,k} \tag{4}$$

where ω is a relaxation factor. A, B, and C are the Jacobian matrices of the flux vectors

$\overline{E}-\overline{E}_v$, $\overline{F}-\overline{F}_v$, and $\overline{G}-\overline{G}_v$, respectively. $\overline{R}^{n+1,k}$ is the residual vector defined as :

$$\overline{R}^{n+1,k} = -\frac{\overline{q}^{n+1,k}-\overline{q}^{n}}{\Delta\tau} - \left(\delta_\xi \overline{E}^{n+1,k} + \delta_\eta \overline{F}^{n+1,k} + \delta_\zeta \overline{G}^{n+1,k}\right) + \left(\delta_\xi \overline{E}_v^{n+1,k} + \delta_\eta \overline{F}_v^{n+1,k} + \delta_\zeta \overline{G}_v^{n+1,k}\right) \tag{5}$$

Note that RHS of Eq. (5) is the same form of discretized momentum equations at '*k*' iteration level. When $\overline{R}^{n+1,k}$ goes to zero, the momentum equations are exactly satisfied at each physical time step. Then, the solution is independent of ω, and any approximations made in the construction of *A*, *B*, and *C*.

Next, in order to solve incompressible flow efficiently, we need a relationship coupling changes in the velocity field with changes in the pressure field while satisfying the divergence-free constraint. In the present study, the Marker-and-Cell (MAC) approach (Viecelli, 1969) was used.

$$\Delta\left(\frac{p}{J}\right) = -\beta\left[\frac{\partial}{\partial\xi}\left(\frac{U-\xi_t}{J}\right) + \frac{\partial}{\partial\eta}\left(\frac{V-\eta_t}{J}\right) + \frac{\partial}{\partial\zeta}\left(\frac{W-\zeta_t}{J}\right)\right]^{n+1,k} \tag{6}$$

where 0and β is a relaxation factor. Again, when Δp goes to zero, the continuity equation is exactly satisfied at each time step. The contravarient velocities in each ξ-, η-, and ζ-direction were denoted as *U*, *V*, and *W*, respectively. ξ_t, η_t, and ζ_t represent the grid speed, obtained by :

$$\begin{aligned}
\xi_t &= -x_\tau\xi_x - y_\tau\xi_y - z_\tau\xi_z \\
\eta_t &= -x_\tau\eta_x - y_\tau\eta_y - z_\tau\eta_z \\
\zeta_t &= -x_\tau\zeta_x - y_\tau\zeta_y - z_\tau\zeta_z
\end{aligned} \tag{7}$$

where $x_\tau\vec{i} + y_\tau\vec{j} + z_\tau\vec{k} = \vec{\Omega}\times\vec{r}$ and $\vec{r}$ denotes the coordinates of each grid point.

The spatial derivatives of convective flux terms are differenced by using upwind QUICK(Quadratic Upstream Interpolation for Convective Kinematics) scheme (Leonard, 1979) to reduce unphysical oscillations for high Reynolds number flows, and the spatial derivatives of viscous terms and continuity equation are differenced with central difference. The fourth order artificial damping term is added to the continuity equation only. To capture the turbulent flows, low Reynolds number k-ε model (Chien, 1982) is employed.

3 Initial and boundary condition

The governing equations are solved in the inertial frame. The use of inertial frame simplifies the governing equations because centrifugal and Coriolis force do not appear explicitly. This approach is suitable for rotating propellers and turbomachinery. Since it is assumed that the rotor is impulsively rotated from rest, the rest condition is used as initial condition and farfield boundary condition. At outflow boundary, the velocity is

extrapolated from interior nodes to account for the removal of vorticity from the flow domain by convective processes. On the body surface, the no slip condition is applied for velocity components. The surface pressure is determined by setting the zero normal gradient of pressure, i.e., $\partial p / \partial n = 0$. To handle interface boundary of block between rotor and stator, the sliding multiblock technique (Park et al, 1996) using cubic spline interpolation and bilinear interpolation technique were applied in 2-D and 3-D interface plane, respectively.

4 Results and discussion

Since the ducted marine propulsor with rotor-stator interactions does not have any published experimental or numerical data, the turbine flow with rotor-stator interaction was simulated to validate the present code.

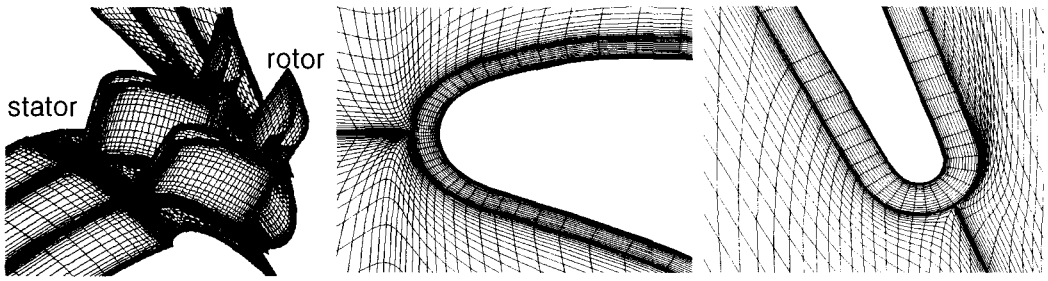

(a) Grid system (b) Leading edge of stator (c) Trailing edge of stator

Figure 1: Rotor-stator grid system of a turbine

Figure 1 shows H-grid system embedded by O-grid near the blade surface of rotor and stator. This embedded O-grid can eliminate the branch cut problem of H-grid at leading edge and trailing edge and, thus, increase accuracy and robustness. The calculations were performed at two rotating speeds of C_x/U =0.68 and 0.78, where C_x is the absolute inflow speed and U is the rotating speed of rotor at mid-span. Figure 2 shows time averaged pressure coefficients on the rotor surface at the mid-span, compared with experiment (Dring et al, 1982). This figure shows a good agreement with each other.

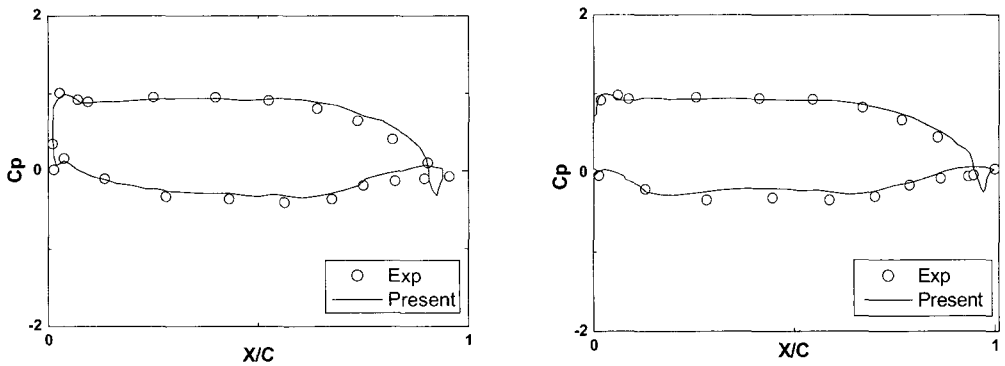

(a)At $C_x/U = 0.68$ (b) At $C_x/U = 0.78$

Figure 2: Time averaged Cp at the mid-span of rotor

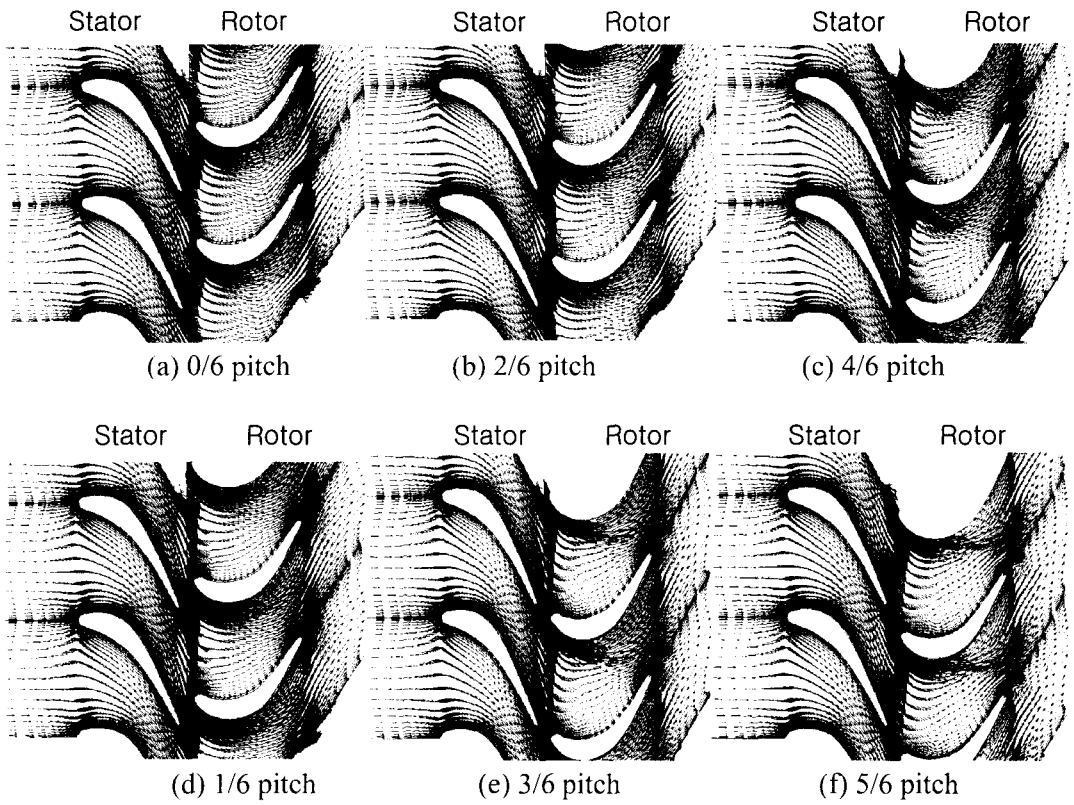

Figure 3: Velocity vectors at every 1/6 - pitch movement ($C_x/U = 0.78$)

Figure 3 shows the velocity vectors at C_x/U =0.78, plotted at each 1/6-pitch movement of the rotor. In this figure, unsteady flow feature of the rotor is evidently shown, while the flow around the stator is relatively steady. Especially in Figure 3 (d)-(f), the strong jet-like flow on the suction side of the rotor is shown. This is because the high speed flow which attains its high speed while passing over the suction side of the stator passes again over the suction side of the rotor and, consequently, obtains more high speed. This high speed flow over the suction side of the rotor is shown as the strong jet-like flow in Figure 3 (d)-(f).

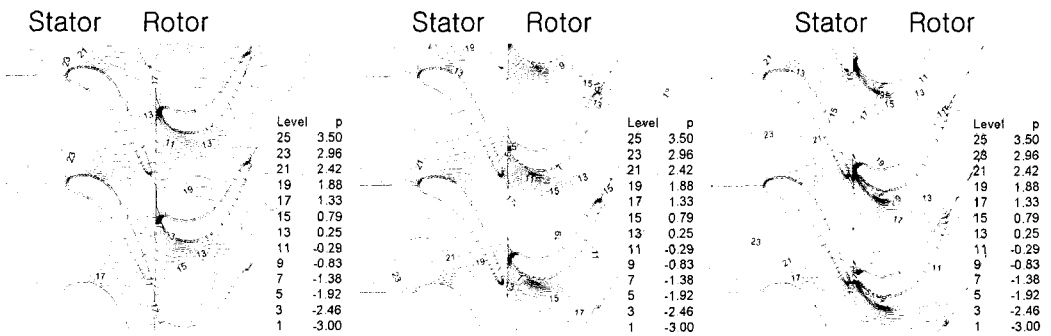

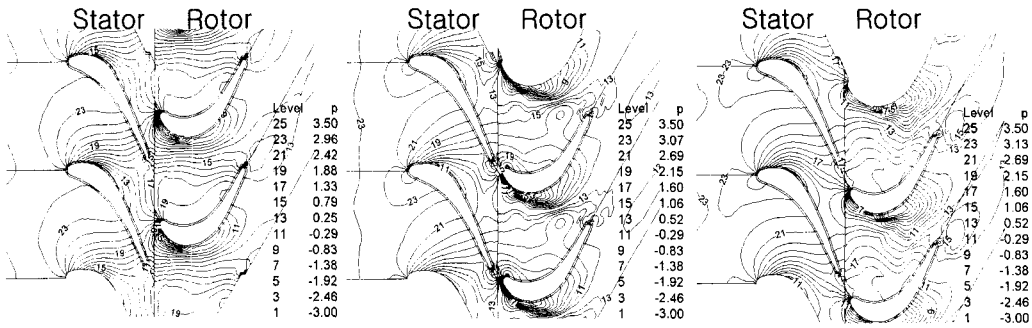

(d) 1/6 pitch (e) 3/6 pitch (f) 5/6 pitch

Figure 4: Pressure contours at every 1/6 – pitch movement ($C_x / U = 0.78$)

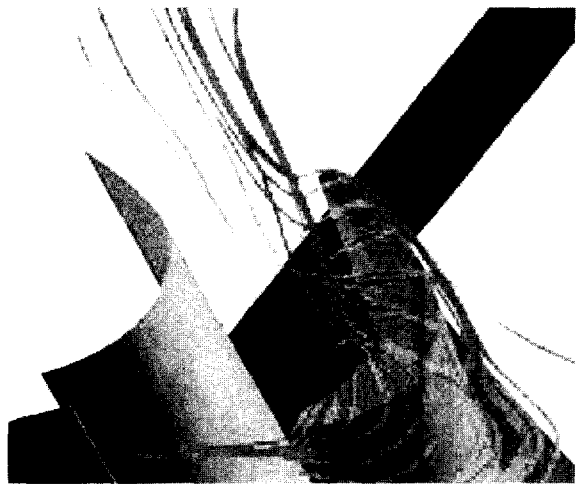

Figure 5: Streamlines and tip vortex

Figure 4 shows the pressure contours. Figure 5 shows the tip vortex generated on the rotor. After the code validation, the present method has been applied to the flow around a single-stage ducted marine propulsor at 5×10^5 of Reynolds number based on the chord length of the rotor and at 0.833 of advance ratio. Figure 6 shows configuration and grid

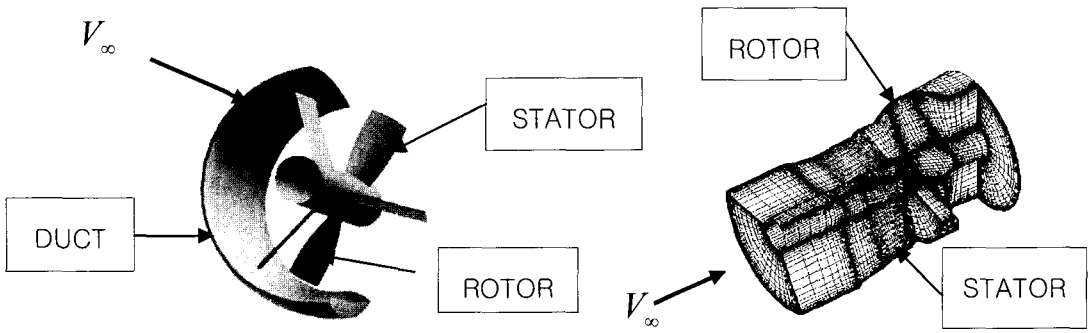

(a) Configuration (b) Grid system

Figure 6: Configuration and grid of ducted marine propulsor

of the ducted marine propulsor. The proplusor consists of a two-bladed rotor, a three-bladed stator, and an annular duct as shown in Figure 6(a). The detail data of geometry were given by Hughes (1993). The airfoil shape of rotor and stator are modified NACA 66-series without skew and rake. The hub has a constant radius equal to 25% of the rotor radius. The tip clearance between the duct and the rotor tip is 0.5% of the rotor radius. The gap between the rotor and the stator is 93% on the average, based on the chord length of the rotor. The multiblocked grid around the propulsor was generated by an elliptic grid generator. The whole grid consists of five blocks and the number of grid points of each blocks are 51×41×33, 63×30×33, 41×5×9, 34×61×21, and 40×51×43, respectively. Figure 7 shows surface pressure coefficients (time averaged) at r/R=0.3, 0.5, 0.7, and 0.9, where R denotes the radius of the rotor tip.

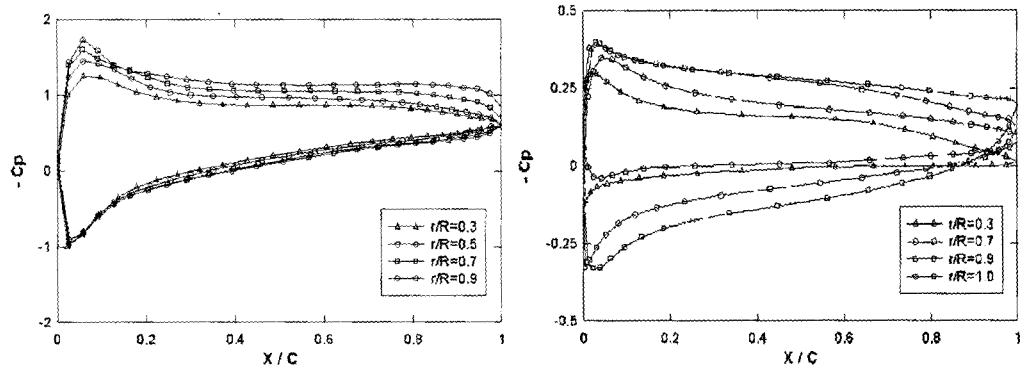

(a) On the stator surface (b) On the rotor surface

Figure 7: Surface pressure coefficients (time-averaged) at four different radii

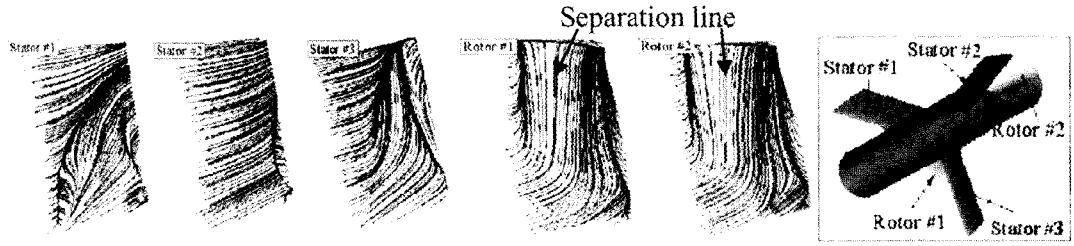

(a)On the stator (b) On the rotor (c)Position of rotor

Figure 8: Instantaneous limiting streamlines on the suction side of rotor and stator

The instantaneous limiting streamlines at the suction side of stator and rotor are shown in Figure 8, where the rotor No.1 is located at about midway of stator No.1 and stator No.3. The rotor No.2 is almost in line with stator No.2 as shown in Figure 8(c). This figure indicates that the flow feature of the stator strongly depends on the closeness to the rotor. In Figure 8(a), the flow patterns of stator No.1, 2, and 3 are different each other, while those of rotor No.1 and 2, as shown in Figure 8(b), are relatively similar. The streamlines of stator No. 2 of Figure 8(a) are much straightened compared with those of stator No. 1 and No. 3, because stator No. 2 is aligned with rotor No. 2. Consequently, rotor No. 2 strongly draws the fluid of stator No. 2. Figure 8(b) also shows the strong centrifugal force effects acting on the fluid particle of the rotating rotor and the separation line generated by tip vortex. Figure 9 shows the velocity component of axial, tangential, and radial direction

in the location of just ahead of the stator, in the middle of gap, and just behind of the rotor. Here, suction side and pressure side of the rotor are placed at 0° and 180° azimuthal angle, respectively. Those of stator are placed at 0° and 120° azimuthal angle. The ordinate of this figure, nondimensional velocities, denotes the velocity components nondimensionalized by free stream velocity. As expected, in Figure 9(a) of which location is just ahead of the stator, only axial component of velocity, without tangential and radial component, exists in inboard span of the stator. The negative value of radial component at r/R=0.9 is due to the inward flow effects of the duct. As the flow passes over the stator, it attains tangential and radial component of velocity, as shown in Figure 9(b). Figure 9(c) shows the increment of axial velocity component due to the push-action of the rotor. Also, the swirl is still shown behind the rotor because the stator has constant pitch angle that is not suitable to eliminate the swirl component entirely and to straighten the downstream flow. If the pitch angle of the stator is variable along the radial direction and very well designed, the flow behind the rotor may be straightened without swirl component.

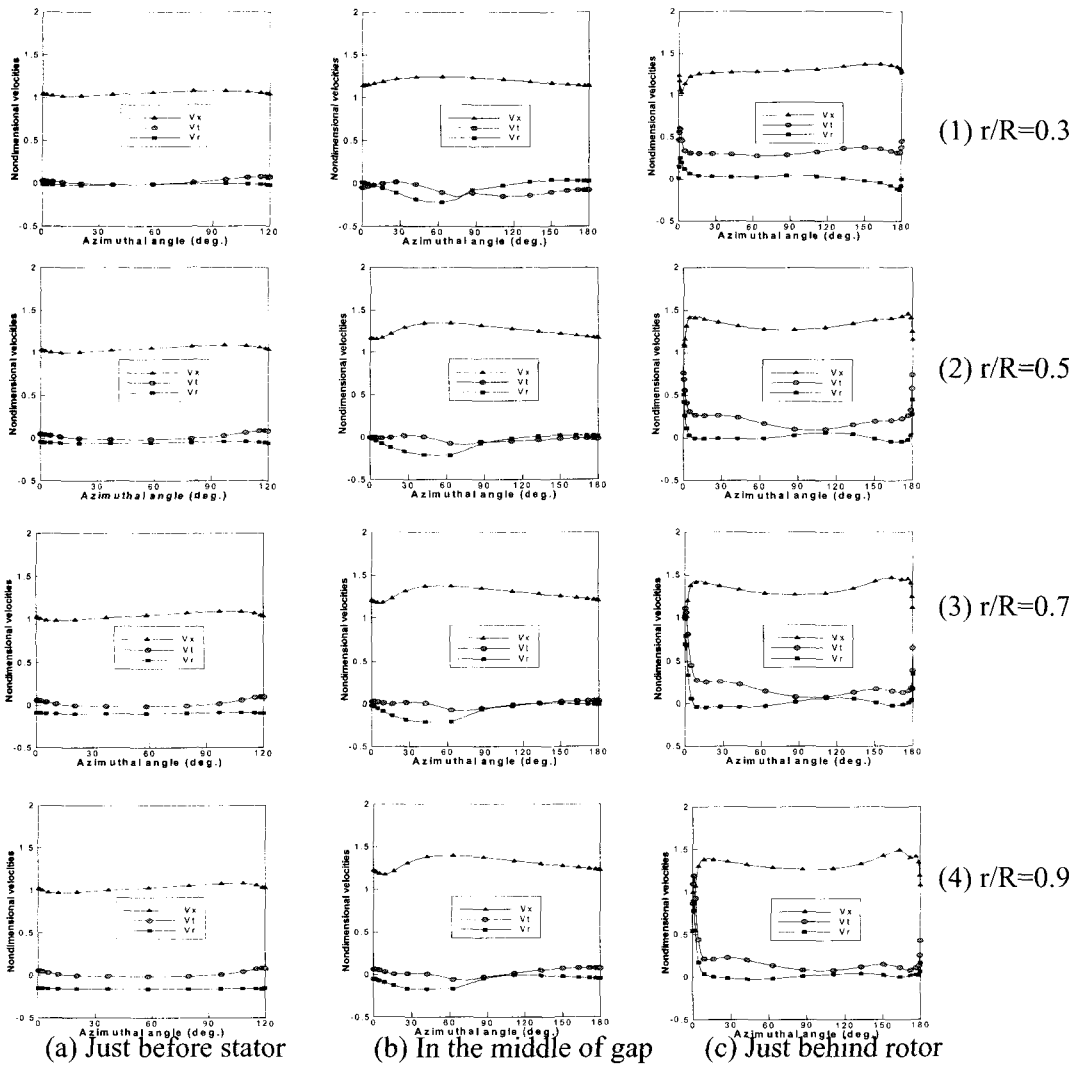

Figure 9: Distributions of velocity components

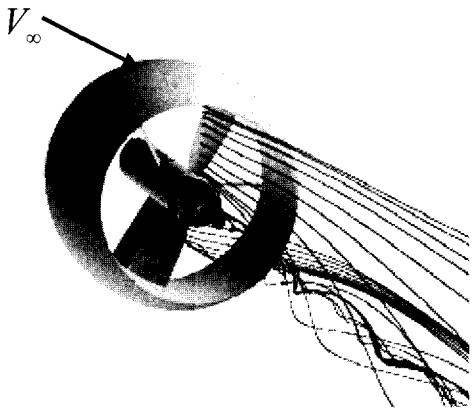

Figure 10: Streamlines emanating from the rotor plane

Figure 10 shows streamlines emanating from the rotor plane. The strong hub vortex is evidently shown and the swirl component of downstream is also shown, as explained in Figure 9(c).

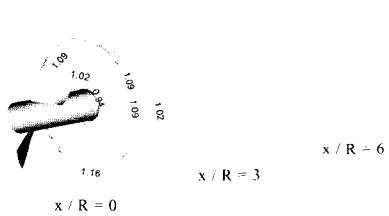

(a) Pressure

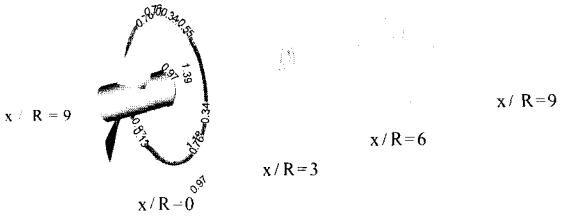

(b) Axial velocity component

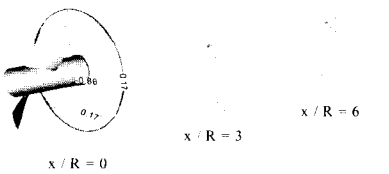

(c) Tangential velocity component

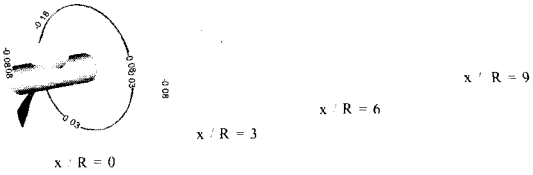

(d) Radial velocity component

Figure 11: Contours of pressure and velocity components in the downstream region

Figure 11 shows the contours of pressure and velocity components in the downstream region. This figure indicates that the pressure and velocity are nearly recovered to the freestream value behind about $x \cong 9R$. For the grid dependency study, Figure 12 shows the variation of propulsive efficiency thrust and torque coefficient with the change of total number of grid points.

$$K_T = \frac{T}{\rho n^2 D^4}; \qquad K_Q = \frac{Q}{\rho n^2 D^5}; \qquad \eta = \frac{J}{2\pi}\frac{K_T}{K_Q} \tag{8}$$

where J denotes the advance ratio. For this grid dependency calculation, three set of grid points are used: 1.8×10^5(coarse), 4.6×10^5(medium), 9.6×10^5(fine). On the fine grid, the converged value of $K_T = 0.104$, $K_Q = 0.024$, and $\eta = 0.56$ were obtained.

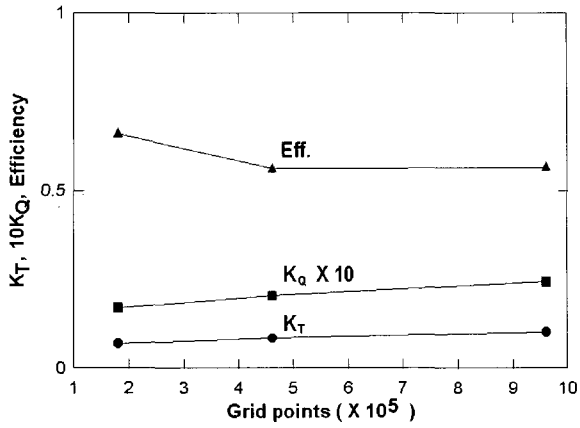

Figure 12: Thrust, torque, and efficiency with changes of grid points

5 Conclusions

The numerical analysis of a single-stage ducted marine propulsor was performed to obtain detailed understanding of complicated three-dimensional viscous flow phenomena including rotor-stator interaction and annular duct effects. 3D incompressible RANS equations were solved on a rotating, nonorthogonal body-fitted multiblocked grid system. To handle interface boundary between rotor and stator, the sliding multiblock method was applied. To validate present code, a turbine flow was simulated. Time averaged pressure coefficient was compared with experiment and a fairly good agreement has been obtained. After the code validation, the flowfield around a single-stage ducted marine propulsor was simulated and, then, pressure distributions, streamlines, and changes of velocity components were plotted. The hydrodynamic coefficients and propulsive efficiency were also obtained.

Acknowledgement

This work was supported by Advanced Ship Engineering Research Center of the Korea Science and Engineering Foundation.

References

Chen, J.P. and D.L. Whitfield. 2000. Computation of rotor-stator of interaction using the Navier-Stokes Equations. Final Report MSSU-COE-ERC-00-12.

Chien, K.Y. 1982. Prediction of channel and boundary-layer flows with a low-Reynolds-number turbulent model. AIAA Journal, **20, 1**, 33-38.

Dring, R.P., H.D. Joslyn, L.W. Hardin and J.H. Wagner. 1982. Turbine rotor-stator

interaction. Journal of Engineering for Power, **104**, 729-742.

Hassan, K.K., S. Abdallah and Y.T. Lee. 1995. Three-dimensional solutions for incompressible turbulent flow in a high Reynolds number pump. Numerical Simulations in Turbomachinery, ASME-FED, **227**, 109-116.

Hughes, M.J. 1993. Analysis of multi-component ducted propulsors in unsteady flow. Ph. D. Thesis. Department of Ocean Engineering, MIT.

Kerwin, J.E., S.A. Kinnas, J.T. Lee and W.Z. Shih. 1987. A surface panel method for the hydrodynamic analysis of ducted propellers. Trans. SNAME, **95**.

Kinnas, S.A. and W.B. Coney. 1992. The generalized image model – an application to the design of ducted propellers. Journal of Ship Research, **36, 3**, 197-209.

Lee, Y.T., C. Har and J. Loellbach. 1994. Flow analyses in a single-stage propulsion pump. ASME Paper, 94-GT-139.

Leonard, B.P. 1979. A stable and accurate convective modelling procedure based on quadratic upstream interpolation. Computer Methods in Applied Mechanics and Engineering, **19**, 59-98.

Park, W.G. and L.N. Sankar 1991. An iterative time marching procedure for unsteady viscous flows. ASME BED, **20**, 281-284.

Park, W.G. and L.N. Sankar 1993. Numerical simulation of incompressible viscous flow around a marine propeller. AIAA Paper, 93-3503.

Park, W.G., H.W. Kim, Y.R. Jung, K.S. Kim and E.D. Park. 1996. Unsteady incompressible turbulent flow simulation of the rotor-stator configuration. Proceedings of the 6th International Symposium on Transport Phenomena and Dynamics of Rotating Machinery. **2**, 257-267.

Park, W.G., Y.R. Jung and S.D. Ha. 1998. Numerical viscous flow analysis around a high speed train with crosswind effects. AIAA Journal. **36, 3**, 477-479.

Sheng, C., J.P. Chen, L.K. Taylor, M.Y. Jiang and D.L. Whitfield. 1997. Unsteady multigrid method for simulating 3-d incompressible Navier-Stokes flows on dynamic relative motion grids. AIAA Paper, 97-04461997.

Viecelli, J.A. 1969. A method for including arbitrary external boundaries in the MAC incompressible fluid computing technique. J. of Computational Physics, **4,** 543-551.

Zierke, W.C., W.A. Straka and P.D. Taylor. 1995. An experimental investigation of the flow through an axial-flow pump. J. of Fluids Engineering. **117**, 485-490.

Zierke, W.C. and W.A. Straka. 1996. Flow visualization and the three-dimensional flow in an axial-flow pump. J. of Propulsion and Power, **12, 2**, 250-259.